Journal of Sound and Vibration (1998) **218**(2), 307–331
Article No. sv981842

MODAL ANALYSIS OF FLEXIBLE BEAMS WITH DELAYED RESONATOR VIBRATION ABSORBER: THEORY AND EXPERIMENTS

N. Olgac and N. Jalili

Mechanical Engineering Department, *University of Connecticut*, *Storrs*, *CT* 06269-3139 *U.S.A.*

(*Received* 19 *November* 1997, *and in final form* 6 *July* 1998)

A recent active vibration absorption method, the Delayed Resonator (DR) is considered. The DR absorber is implemented on a flexible beam, and the dynamic features of this structure are studied. An analytical model of the system is developed in order to predict the experimental findings. Instead of the earlier finite difference method, modal co-ordinate representation is adopted here. In particular, the stability features obtained through analytical and experimental studies are compared. The boundary conditions (BCs), i.e., the beam's clamping structure, dictate the restoring forces on the beam–absorber system, and therefore, play an important role on the system stability. In the experimental work the results are generated under the present beam BCs. For the analytical study, however, they have to be carefully formulated. In order to reflect the physical reality some unconventional BCs are used on the beam. This forms an important part of the "modelling" effort presented here. The results obtained concur with the experimental findings better than the earlier dynamic models which use the finite difference method and ideal clamped–clamped BCs. In summary, modal representation with the unconventional BCs are suggested as an analytical tool for the design of DR absorbers operating on beams.

1. INTRODUCTION

A recent active vibration absorption strategy, the Delayed Resonator (DR), is considered when operated on a flexible beam [1, 2]. The primary objective of this report is to present an analytical design tool to assess the stability properties of the controlled system.

The DR vibration absorber has some attractive features in eliminating tonal vibrations from the objects to which it is attached [2–4]. Some of them are: real-time tunability, the stand-alone nature of the actively controlled absorber, and the simplicity of the application. Additionally, this single-degree-of-freedom (SDOF) absorber can also be tuned to handle multiple frequencies of vibration [4].

0022–460X/98/470307 + 25 $30.00/0

It is particularly important that the combined system, i.e., the primary structure and the absorber together, is asymptotically stable when the DR is implemented on a flexible beam. The experimental efforts conducted to date offer encouraging results. Earlier analytical studies on this setting show reasonable correspondence to the experiments for most of the tonal frequency ranges. However, they fall short of supporting the experiments for the multiple frequency vibration suppression cases. This study expands the analytical effort, leading to a new tool of assessing the performance of DR absorption methods which yield a better match with the experiments.

The earlier modelling investigations were based on the Finite Difference Method (FDM) representation of the flexible body [5]. This approach had limited success in extracting higher order properties of vibration suppression with DR. The analytical effort disagreed with the experimentally stable operation of the "Dual-Frequency Fixed Delayed Resonator" (DFFDR) [4, 6]. This short-fall originated from not only discritization errors incurring in the FDM representation of the flexible dynamics but also unrealistically simplified selection of the boundary conditions (BCs). In this work we remove both elements utilizing the Ritz–Galerkin representation of the beam and absorber dynamics, and some unconventional BCs.

Modal representation of flexible beams is adopted from the common literature [7–10]. Two critical modelling decisions are treated first: (a) the number of modes to be included in the model, and (b) appropriate form of the BCs for the mode shapes (i.e., the eigenfunction determinations). The discrete component attachments, the DR absorber and the exciter are included. The stability of this combined system is then studied and the results are compared with the experimental findings.

The main structure is taken as a clamped–clamped Euler–Bernoulli beam. As known from practice, the actual BCs do not comply with the ideal zero slope and zero deflection at the end points. In reality some compliance in lateral and bending directions is always present. Therefore, the boundary conditions in the analytical model are formed appropriately to better represent reality.

The paper contains the following. The delayed resonator is briefly reviewed in section 2 with inclusion of acceleration feedback. The double frequency suppression ability of the DR, dual frequency fixed delayed resonator, is also summarized. Section 3 addresses the governing equations of motion for DR on a flexible beam. The issue of stability is also addressed in this section. Effect of the BCs on the beam dynamics, as the primary structure, is analyzed in section 4. Experimental set-up and numerical results are compared in sections 5 and 6. Section 7 concludes the study and points out future research.

2. DELAYED RESONATOR (DR), AN OVERVIEW

The DR vibration absorption technique was recently introduced by references [1, 2]. In order to assist the reader, we present a brief summary of the method. DR has an unconventional control logic which is implemented on a passive absorber

(Figure 1(a)). It consists of a proportional position feedback with time delay. The position feedback can be based on absolute or relative (with respect to the primary) displacements of the absorber [11]. These displacement measurements are prohibitively difficult for high frequency–low amplitude applications. For such cases acceleration feedback is much more feasible. Naturally, the effects of substituting displacement measurements with acceleration should be carefully analyzed.

2.1. DR WITH ACCELERATION FEEDBACK

Consider the reconfigured dynamics of a dissipative mass–spring–damper trio including a proportional delayed acceleration feedback, Figure 1(b). The objective of this feedback control is to convert the dissipative dynamics shown in Figure 1(a) into a conservative (or marginally stable) one with a designated resonance frequency ω_c. In other words, the control aims the placement of dominant poles at $\pm j\omega_c$ for the final system, where $j = \sqrt{-1}$. This pole placement can also be achieved using many other types of *full-state* feedback routines (such as PD). The DR offers simplicity over these techniques due to its form: partial state feedback with delay. This simplicity in implementation, however, yields some complications in stability study, particularly because of the delay introduced in the feedback.

The proposed feedback force to achieve the pole placement is

$$g\ddot{x}_a(t-\tau) \tag{1}$$

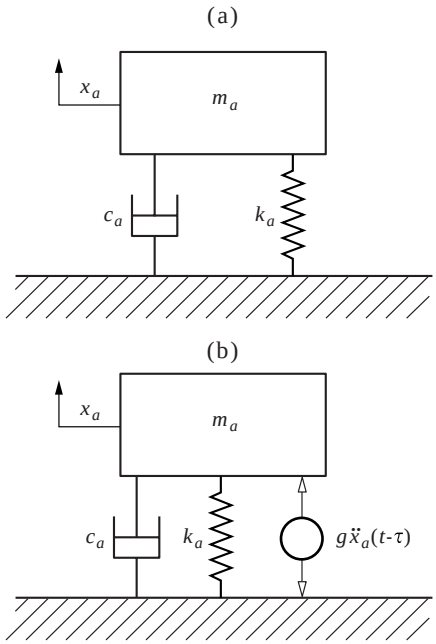

Figure 1. (a) Passive absorber, (b) delayed resonator with acceleration feedback.

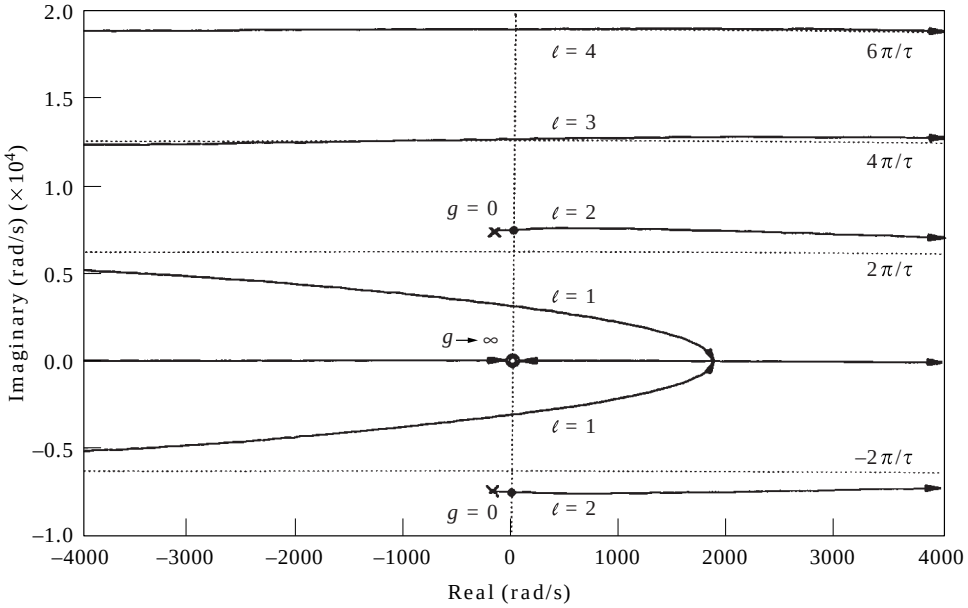

Figure 2. A typical root locus plot for the Delayed Resonator with acceleration feedback, when τ is fixed: $\times$, open loop poles; ●, points of operation; ○, open loop zeros; ▶, increasing gain.

and the corresponding new system dynamics is

$$m_a\ddot{x}_a(t) + c_a\dot{x}_a(t) + k_a x_a(t) - g\ddot{x}_a(t-\tau) = 0. \tag{2}$$

The Laplace domain representation leads to the transcendental characteristic equation

$$m_a s^2 + c_a s + k_a - g s^2 \, \mathrm{e}^{-\tau s} = 0. \tag{3}$$

This equation possesses infinitely many *finite* roots for $g \neq 0$ and $\tau \neq 0$. Their distribution can be sketched following the root locus analysis [5].

To achieve ideal resonator behavior, two dominant roots of equation (3) should be placed on the imaginary axis at the desired crossing frequency ω_c while the others remain in the left-half of the complex plane. Substituting $s = \pm \mathrm{j}\omega_c$ into equation (3) and solving for the control parameters g_c and τ_c one obtains

$$g_c = \frac{1}{\omega_c^2}\sqrt{(c_a\omega_c)^2 + (m_a\omega_c^2 - k_a)^2}, \tag{4}$$

$$\tau_c = \frac{1}{\omega_c}\left\{\tan^{-1}\left[\frac{c_a\omega_c}{m_a\omega_c^2 - k_a}\right] + 2(\ell - 1)\pi\right\}, \qquad \ell = 1, 2, \ldots. \tag{5}$$

The variable parameter ℓ refers to the branch of root loci that happens to cross the imaginary axis at ω_c (Figure 2). Clearly, it does not have to be the first branch.

The practical importance of parameter ℓ is visualized in the plots of $g_c(\omega_c)$ versus $\tau_c(\omega_c)$ and ω_c versus τ_c for varying ℓ values (Figure 3). It is easy to observe that for $\ell = 1$ (i.e., the first branch of root loci crossing the imaginary axis at the desired frequency), the delayed resonance feature can be attained over a semi-infinite frequency range from ω_{A1} to ∞. The lower bound ω_{A1} corresponds to the stability limit of the DR on the first branch. For these g_c and τ_c the second branch crosses to the unstable right half of the complex plane at $j\omega_{A2}$ concurrently with the first branch. In this situation, there are two pairs of roots on the imaginary axis, which impart *dual resonance* in the absorber; it is treated in the next section. If g_c and τ_c are selected to induce $\omega_c < \omega_{A1}$, such as the operating point A_1 in Figure 3, this would result in an unstable root on the second branch, because for the corresponding delay τ_A, the branch no. 2 crosses to the unstable half plane at a smaller gain $g_{A2} < g_{A1}$. Therefore, considering the stability of the *DR alone*, $\omega_{min} = \omega_{A1}$ should be strictly observed.

For $\ell > 1$, following similar reasoning, the range of operating frequencies is limited by both upper and lower bounds due to previous and next branch crossings, respectively. For the common frequency interval of different branches, for instance $\omega_{B2} < \omega_c < \omega_{A2}$ for $\ell = 1$ and 2, both branches can be used for stable DR operation. The $\tau_{C2} = \tau_{C1} + 2\pi/\omega_C$ relation holds between the two feedback delays. However, the gains for both branches remain the same, points D, E, D′ and E′ in Figure 3. This freedom in selecting the parameter ℓ can be considered as a useful tool in the design process of a DR vibration absorber.

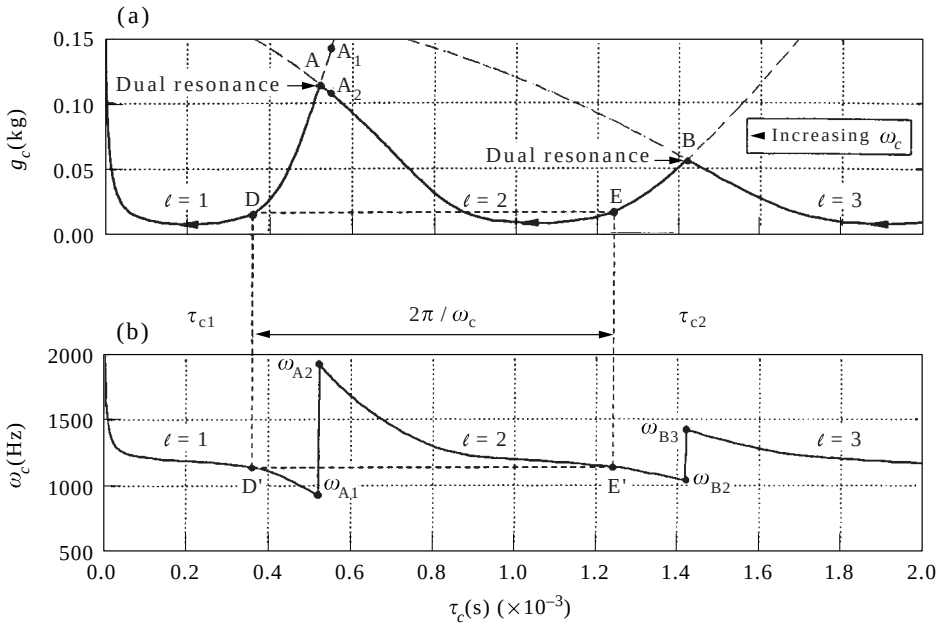

Figure 3. Ranges of operation for Delayed Resonator with acceleration feedback: (a) g_c, (b) ω_c.

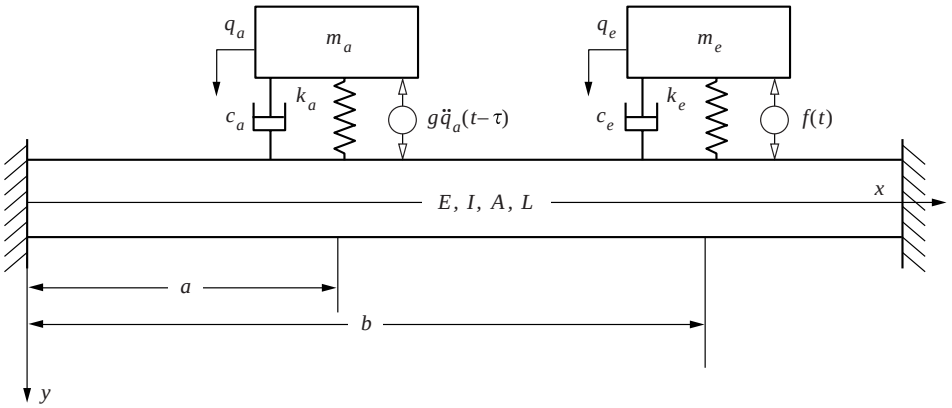

Figure 4. Beam–absorber–exciter system configuration.

2.2. DUAL FREQUENCY FIXED DELAYED RESONATOR (DFFDR)

As explained above, at the stability limits of DR there are two pairs of characteristic roots on the imaginary axis for the same values of g_c and τ_c. Thus, the single-mass DR exhibits two natural frequencies of oscillation simultaneously. This structure is called *Dual Frequency Fixed Delayed Resonator* (*DFFDR*). It acts like two fixed frequency DRs combined in one. Therefore, it is capable of suppressing oscillations emanating from a bitonal (dual frequency) excitation. The details of DFFDR are given in reference [4] for position feedback. This section presents the highlights of a similar DFFDR analysis for acceleration feedback.

In summary, a given absorber (i.e., m_a, k_a, c_a) can be forced into *dual resonance* by a single delayed acceleration feedback $g_c\ddot{x}_a(t-\tau_c)$ provided that all the remaining poles are in the stable left half plane. There exist always some pairs of g_c^* and τ_c^* to achieve this, each pair yields different dual resonance frequencies such as ω_{A1} and ω_{A2}, ω_{B2} and ω_{B3}, etc.; Figure 3. As a point of interest, it is also proved that there is no possibility of creating triple resonance behavior utilizing a similar single delayed feedback, on a single mass absorber [4].

3. DR APPLICATION ON FLEXIBLE BEAMS SYSTEM

Undesirable vibrations of flexible structures have been effectively reduced using a variety of dynamic vibration absorbers. The DR method offers a wide band of absorption frequencies, as well as real-time tunability as two major advantages.

A point to note is that the control logic does not require any information from the primary structure and it is decoupled from the primary system. It is clear, however, that the time delay is a destabilizing factor for the combined system. Forcing a stable mass–spring–damper into a marginally stable resonator brings a complex problem of stability of the combined system into the analysis. This will be addressed in the following sub-sections.

3.1. DERIVATION OF THE GOVERNING EQUATIONS OF MOTION

We consider a general beam as the primary system with DR attached to it and subjected to a harmonic force excitation, as shown in Figure 4. The point excitation is located at b, and the absorber is placed at a. A uniform cross-section is considered for the beam and Euler–Bernoulli assumptions are made. The beam parameters are all assumed to be constant and uniform. To characterize the elastic deformation from the undeformed natural axis of the beam, we use $y(x, t)$. In the derivations that follow, the dot "˙" and prime "′" indicate a partial derivative with respect to the time variable t and position variable x, respectively.

Under these assumptions, the kinetic energy of the system can be written as

$$T = \tfrac{1}{2}\rho \int_0^L \left(\frac{\partial y}{\partial t}\right)^2 \mathrm{d}x + \tfrac{1}{2}m_a\dot{q}_a^2 + \tfrac{1}{2}m_e\dot{q}_e^2. \tag{6}$$

The potential energy of this system using linear strain is given by

$$U = \tfrac{1}{2}EI \int_0^L \left(\frac{\partial^2 y}{\partial x^2}\right)^2 \mathrm{d}x + \tfrac{1}{2}k_a\{y(a, t) - q_a\}^2 + \tfrac{1}{2}k_e\{y(b, t) - q_e\}^2. \tag{7}$$

The equations of motion may now be derived by applying Hamilton's principle. However, to facilitate stability analysis we resort to an assumed-mode expansion and Lagrange's equations. Specifically, y is written as a finite sum, the so-called Galerkin approximation:

$$y(x, t) = \sum_{i=1}^{n} \Phi_i(x) q_{bi}(t). \tag{8}$$

The orthogonality conditions between these mode shapes can also be derived as [12]

$$\int_0^L \rho\Phi_i(x)\Phi_j(x)\,\mathrm{d}x = N_i\delta_{ij}, \qquad \int_0^L EI\Phi_i''(x)\Phi_j''(x)\,\mathrm{d}x = S_i\delta_{ij}, \tag{9}$$

where $i, j = 1, 2, \ldots, n$, δ_{ij} is the Kronecker delta, and N_i and S_i are defined by setting $i = j$ in equation (9). Using the orthogonality conditions, it is possible to rewrite the kinetic and potential energies, i.e., equations (6) and (7), in the more suitable form

$$T = \frac{1}{2}\sum_{i=1}^{n} N_i\dot{q}_{bi}^2 + \tfrac{1}{2}m_a\dot{q}_a^2 + \tfrac{1}{2}m_e\dot{q}_e^2,$$

$$U = \frac{1}{2}\sum_{i=1}^{n} S_i q_{bi}^2 + \tfrac{1}{2}k_a\{y(a, t) - q_a\}^2 + \tfrac{1}{2}k_e\{y(b, t) - q_e\}^2, \tag{10}$$

where N_i and S_i are respective generalized mass and stiffness for the ith mode, as defined above. Also,

$$S_i = N_i \omega_i^2. \tag{11}$$

The acceleration feedback of DR, actuator excitation force, and damping dissipating forces in both DR and exciter are considered as non-conservative forces in Lagrange's formulation. Consequently, the equations of motion are derived. The *absorber* dynamics is governed by

$$m_a \ddot{q}_a(t) + c_a \left\{ \dot{q}_a(t) - \sum_{i=1}^{n} \Phi_i(a) \dot{q}_{bi}(t) \right\}$$

$$+ k_a \left\{ q_a(t) - \sum_{i=1}^{n} \Phi_i(a) q_{bi}(t) \right\} - g \ddot{q}_a(t - \tau) = 0, \tag{12}$$

the *exciter* by

$$m_e \ddot{q}_e(t) + c_e \left\{ \dot{q}_e(t) - \sum_{i=1}^{n} \Phi_i(b) \dot{q}_{bi}(t) \right\} + k_e \left\{ q_e(t) - \sum_{i=1}^{n} \Phi_i(b) q_{bi}(t) \right\} = -f(t), \tag{13}$$

and finally the *beam*:

$$N_i \ddot{q}_{bi}(t) + S_i q_{bi}(t) + c_a \left\{ \sum_{i=1}^{n} \Phi_i(a) \dot{q}_{bi}(t) - \dot{q}_a(t) \right\} \Phi_i(a) + c_e \left\{ \sum_{i=1}^{n} \Phi_i(b) \dot{q}_{bi}(t) \right.$$

$$\left. - \dot{q}_e(t) \right\} \Phi_i(b) + k_a \left\{ \sum_{i=1}^{n} \Phi_i(a) q_{bi}(t) - q_a(t) \right\} \Phi_i(a) + k_e \left\{ \sum_{i=1}^{n} \Phi_i(b) q_{bi}(t) \right.$$

$$\left. - q_e(t) \right\} \Phi_i(b) + g \Phi_i(a) \ddot{q}_a(t - \tau) = f(t) \Phi_i(b), \qquad i = 1, 2, \ldots, n. \tag{14}$$

Equations (12), (13) and (14) form a system of $n + 2$ second order coupled differential equations.

By proper selection of the feedback gain $g = g_c$ and delay $\tau = \tau_c$, as in equations (4) and (5), the DR can be tuned to the desired resonant frequency ω_c. This selection satisfies the transcendental characteristic equation (3) for $s = \pm \mathrm{j}\omega_c$. This condition, in turn, forces the beam to be motionless at a, when the beam is excited by a tonal force at frequency ω_c. This conclusion is arrived at by taking the Laplace transform of equation (12) and using equation (3). In short,

$$Y(a, s) = \sum_{i=1}^{n} \Phi_i(a) Q_{bi}(s) = 0, \tag{15}$$

where $Y(a, s) = \mathscr{L}\{y(a, t)\}$ and $Q_{bi}(s) = \mathscr{L}\{q_{bi}(t)\}$. Equation (15) can be rewritten in the time domain as

$$y(a, t) = \sum_{i=1}^{n} \Phi_i(a) q_{bi}(t) = 0, \tag{16}$$

which indicates that the steady state vibration of the point of attachment of the absorber is eliminated. The absorber mimics a resonator at the frequency of excitation, and absorbs all the vibratory energy at the point of attachment.

3.2. STABILITY OF THE COMBINED SYSTEM

In the preceding section, we have derived the equations of motion for the beam–exciter–absorber system, in its most general form. As stated before, inclusion of the delay element in the system is, indeed, an invitation to instability. This topic is treated next.

The equations of motion, i.e., equations (12), (13) and (14), can be rewritten in the Laplace domain. For the absorber:

$$(m_a s^2 + c_a s + k_a - g s^2 \, \mathrm{e}^{-\tau s}) Q_a(s) - (c_a s + k_a) \left[\sum_{i=1}^{n} \Phi_i(a) Q_{bi}(s) \right] = 0; \tag{17}$$

for the exciter:

$$(m_e s^2 + c_e s + k_e) Q_e(s) - (c_e s + k_e) \left[\sum_{i=1}^{n} \Phi_i(b) Q_{bi}(s) \right] = -F(s); \tag{18}$$

and for the beam (using equations (17) and (18)):

$$(N_i s^2 + S_i) Q_{bi}(s) + m_a \Phi_i(a) s^2 Q_a(s) + m_e \Phi_i(b) s^2 Q_e(s) = 0, \qquad i = 1, 2, \ldots, n. \tag{19}$$

At this stage structural and viscous damping terms are introduced by replacing S_i with complex stiffness $S_i(1 + j\delta)$ and appending a cs term, respectively. That is, the new S_i becomes

$$S_i(1 + \mathrm{j}\delta) + cs, \tag{20}$$

where S_i is defined in equation (9).

Hence, the Laplace domain representation of the combined system takes the form

$$\mathbf{A}(s)\mathbf{Q}(s) = \mathbf{F}(s), \tag{21}$$

where

$$\mathbf{Q}(s) = \left\{ \begin{array}{c} Q_a(s) \\ Q_e(s) \\ Q_{b_1}(s) \\ \vdots \\ Q_{bn}(s) \end{array} \right\}_{(n+2)\times 1}, \qquad \mathbf{F}(s) = \left\{ \begin{array}{c} 0 \\ -F(s) \\ 0 \\ \vdots \\ 0 \end{array} \right\}_{(n+2)\times 1},$$

$$\mathbf{A}(s) = \left[\begin{array}{ccccc} m_a s^2 + c_a s + k_a - g s^2 \, \mathrm{e}^{-\tau s} & 0 & -\Phi_1(a)(c_a s + k_a) & \cdots & -\Phi_n(a)(c_a s + k_a) \\ 0 & m_e s^2 + c_e s + k_e & -\Phi_1(b)(c_e s + k_e) & \cdots & -\Phi_n(b)(c_e s + k_e) \\ m_a \Phi_1(a) s^2 & m_e \Phi_1(b) s^2 & N_1 s^2 + cs + S_1(1 + \mathrm{j}\delta) & \cdots & 0 \\ \vdots & \vdots & \vdots & \ddots & \vdots \\ m_a \Phi_n(a) s^2 & m_e \Phi_n(b) s^2 & 0 & \cdots & N_n s^2 + cs + S_n(1 + \mathrm{j}\delta) \end{array} \right]. \tag{22}$$

In order to assess the combined system stability, the roots of the characteristic equation, $\det(\mathbf{A}(s)) = 0$ are analyzed. The presence of transcendental delay term in the characteristic equations complicates this effort. The root locus plot observation mentioned in section 2 as depicted in Figure 2 for DR alone can now be applied to the entire system. This process constitutes the primary objective of the work presented here.

It is typical that increasing feedback gain, g_c, causes instability as the roots move from left to right in the complex plane. Consequently, for a given delay τ, the gain corresponding to the DR operation should be smaller than the gain for which the global system becomes marginally stable using the same delay, τ. The ratio of these two gains $g_{cs}(\tau)/g_c(\tau)$ can be defined as the *stability margin* of the control system, at that delay value τ. The comparison of $g_{cs}(\omega_c)$ versus $\tau_{cs}(\omega_c)$ plot of the combined system with the $g_c(\omega_c)$ versus $\tau_c(\omega_c)$ plot of the DR reveals this gain margin for the entire frequency spectrum. This picture also yields the frequency range for stable operation of the combined system. That is, for a given τ_c the system is stable if $g_c < g_{cs}$ or the stability margin is greater than one. An example of such treatment is presented in the numerical section below.

4. EFFECT OF BEAM BOUNDARY CONDITIONS

We present an essential analysis, next, on the determination of the eigenfunctions, or mode shapes $\Phi_i(x)$, as a review. When all external forces are zero, the classical Euler–Bernoulli equation represents the beam dynamics.

$$\rho \frac{\partial^2 y}{\partial t^2} + EI \frac{\partial^4 y}{\partial x^4} = 0. \tag{23}$$

Substituting the Galerkin approximation of equation (8) into the equation (23) forms an expression for the eigenfunction $\Phi_i(x)$ as

$$\Phi_i(x) = \alpha_1 \sin \kappa_i x + \alpha_2 \cos \kappa_i x + \alpha_3 \sinh \kappa_i x + \alpha_4 \cosh \kappa_i x, \qquad i = 1, 2, \ldots, n, \tag{24}$$

where κ_i is the modified spatial frequency which is defined as

$$\kappa_i^2 = \omega_i \sqrt{\frac{\rho}{EI}}, \qquad i = 1, 2, \ldots, n. \tag{25}$$

It is convenient to write these eigenfunctions in the following form to implement the homogenous BCs:

$$\begin{aligned} \Phi_i(x) = {} & C_1(\cos \kappa_i x + \cosh \kappa_i x) + C_2(\cos \kappa_i x - \cosh \kappa_i x) \\ & + C_3(\sin \kappa_i x + \sinh \kappa_i x) + C_4(\sin \kappa_i x - \sinh \kappa_i x). \end{aligned} \tag{26}$$

4.1. CLAMPED–CLAMPED BEAM DYNAMICS

Next, two sets of BCs are considered. The first set is for the conventional clamped–clamped case as was treated in the earlier FDM study [5], for which the BCs are

$$\left.\begin{matrix}\Phi = 0\\ \Phi' = 0\end{matrix}\right|_{x=0}, \qquad \left.\begin{matrix}\Phi = 0\\ \Phi' = 0\end{matrix}\right|_{x=L}. \tag{27}$$

Using these BCs in the eigenfunctions of equation (26), one obtains

$$\Phi_i(x) = H_i[\cos \kappa_i x - \cosh \kappa_i x + R_i(\sin \kappa_i x - \sinh \kappa_i x)]. \tag{28}$$

H_i is determined by normalizing the amplitude of vibration in each mode, and R_i is given by [13]

$$R_i = -\frac{\cos(\kappa_i L) - \cosh(\kappa_i L)}{\sin(\kappa_i L) - \sinh(\kappa_i L)} = \frac{\sin(\kappa_i L) + \sinh(\kappa_i L)}{\cos(\kappa_i L) - \cosh(\kappa_i L)}, \tag{29}$$

where

$$\kappa_i \approx \frac{(2i+1)\pi}{2L}, \qquad i = 1, 2, \ldots, n. \tag{30}$$

Notice that two of the integration constants in equation (26) conveniently become zero.

4.2. PARTIALLY CLAMPED–CLAMPED BEAM DYNAMICS

As indicated in reference [5] the stability charts which are obtained analytically (using the FDM representation) with clamped–clamped BCs were not in full agreement with those generated experimentally. One of the major reasons for this is, indeed, inevitable imperfections in clamping of the beam at the end points which were not taken into account in the modelling. This is resolved next by considering a beam with general elastic BCs.

In order to analyze the problem, a uniform beam is considered, as depicted in Figure 5. k_{TR} and $k_{\theta R}$, k_{TL} and $k_{\theta L}$ are the transverse stiffness, and the torsional stiffness constants, at the left and right end of the beam, respectively. When these spring constants are selected as combinations of infinity or zero, a variety of ideal BCs result. For symbolic simplification, we define the following non-dimensional spring constants:

$$\beta_1 = \frac{k_{\theta L} L}{EI}, \qquad \beta_2 = \frac{k_{TL} L^3}{EI}, \qquad \beta_3 = \frac{k_{\theta R} L}{EI}, \qquad \beta_4 = \frac{k_{TR} L^3}{EI}. \tag{31}$$

The associated general *BC* expressions for the governing differential equation of the system (23) are in the form of [14]

$$\text{at } x = 0, \begin{cases} \Phi''(x) - \dfrac{\beta_1}{L}\Phi'(x) = 0, \\ \Phi'''(x) + \dfrac{\beta_2}{L^3}\Phi(x) = 0, \end{cases} \quad \text{and at } x = L, \begin{cases} \Phi''(x) + \dfrac{\beta_3}{L}\Phi'(x) = 0, \\ \Phi'''(x) - \dfrac{\beta_4}{L^3}\Phi(x) = 0. \end{cases} \tag{32}$$

Inserting the eigenfunctions (26) into the BCs (32), one obtains a set of four homogenous equations in terms of C_1, C_2, C_3, and C_4, given by

$$\begin{bmatrix} 0 & 1 & \frac{\beta_1}{\kappa L} & 0 \\ \frac{\beta_2}{(\kappa L)^3} & 0 & 0 & -1 \\ -C + Ch - \frac{\beta_3}{\kappa L}(S - Sh) & -C - Ch - \frac{\beta_3}{\kappa L}(C + Ch) & -S + Sh + \frac{\beta_3}{\kappa L}(C + Ch) & -S - Sh - \frac{\beta_3}{\kappa L}(C - Ch) \\ S + Sh - \frac{\beta_4}{(\kappa L)^3}(C + Ch) & S - Sh - \frac{\beta_4}{(\kappa L)^3}(C - Ch) & -C + Ch - \frac{\beta_4}{(\kappa L)^3}(S + Sh) & -C - Ch - \frac{\beta_4}{(\kappa L)^3}(S + Sh) \end{bmatrix} \begin{Bmatrix} C_1 \\ C_2 \\ C_3 \\ C_4 \end{Bmatrix} = \mathbf{0}, \tag{33}$$

where κL is the non-dimensional natural frequency and

$$C = \cos(\kappa L), \qquad S = \sin(\kappa L), \qquad Ch = \cosh(\kappa L), \qquad Sh = \sinh(\kappa L). \quad (34)$$

The determinant of the coefficient matrix is set to zero to obtain the characteristic equation, from which the non-dimensional natural frequencies, κL, can be determined. Consequently, the eigenfunctions necessary for the Galerkin representation of equation (8) can readily be formed.

However, the characteristic equation in this general form is very complicated to solve. One can rewrite this equation as

$$\tilde{a}\beta_1\beta_2\beta_3\beta_4 + \tilde{b}\beta_1\beta_3(\beta_2 + \beta_4) + \tilde{c}\beta_2\beta_4(\beta_1 + \beta_3) + \tilde{d}(\beta_1\beta_2 + \beta_3\beta_4)$$
$$+ \tilde{e}(\beta_1\beta_4 + \beta_2\beta_3) + \tilde{f}\beta_1\beta_3 + \tilde{g}\beta_2\beta_4 + \tilde{h}(\beta_1 + \beta_3) + \tilde{k}(\beta_2 + \beta_4) + \tilde{l} = 0, \quad (35)$$

where coefficients $\tilde{a}, \tilde{b}, \tilde{c}, \ldots$ are trigonometric functions of the non-dimensional frequency κL. They are given in Appendix A for the interested reader.

Equation (35) represents a general form of the characteristic equation for a uniform Euler–Bernoulli beam. As stated earlier, setting the stiffness constants β_1, β_2, β_3 and β_4 to zero or infinity, all combinations of the ideal BCs can be obtained. For instance, for a clamped–clamped beam all β_i are infinity and equation (35) is reduced to

$$\tilde{a} = 1 - CCh = 0. \quad (36)$$

In another example for the clamped–free beam, β_1 and β_2 are infinity and β_3 and β_4 are zero. This yields

$$\tilde{d} = (\kappa L)^4(1 + CCh) = 0 \Rightarrow 1 + CCh = 0. \quad (37)$$

These two characteristic equations are in full agreement with the common literature, for the conventional BCs [12].

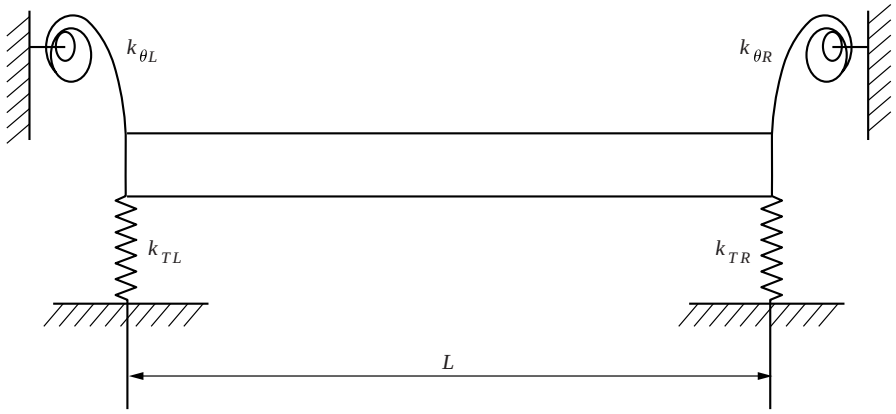

Figure 5. Beam with elastic boundary conditions.

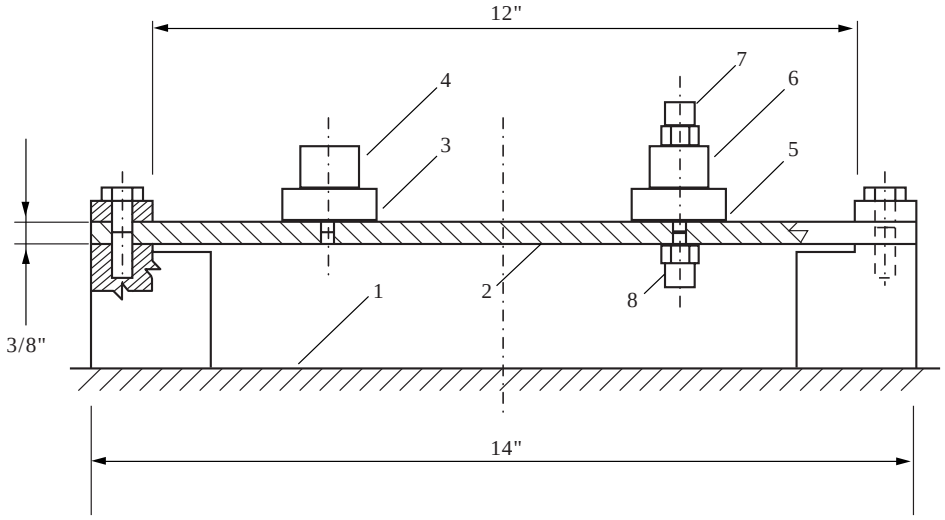

Figure 6. Experimental structure, steel $E = 210$ GPa.

Using equation (33) in equation (26), one can obtain the eigenfunction $\Phi_i(x)$ in the form

$$\Phi_i(x) = H_i\Bigg\{\cos\kappa_i x - \cosh\kappa_i x - \frac{\kappa_i L}{\beta_1}(\sin\kappa_i x + \sinh\kappa_i x) + R_i\left[\sin\kappa_i x - \sinh\kappa_i x + \frac{(\kappa_i L)^3}{\beta_2}(\cos\kappa_i x + \cosh\kappa_i x)\right]\Bigg\}, \tag{38}$$

where H_i is determined by normalizing the amplitude of vibration, as in an ideal clamped–clamped case, and R_i is given by

$$R_i = \frac{C + Ch + (\beta_3/\kappa_i L)(S + Sh) + (\kappa_i L/\beta_1)[-S + Sh + (\beta_3/\kappa_i L)(C + Ch)]}{-S - Sh + (\beta_3/\kappa_i L)(C - Ch) + ((\kappa_i L)^3/\beta_2)[-C + Ch - (\beta_3/\kappa_i L)(S - Sh)]}. \tag{39}$$

Setting all β_i to infinity, one can reduce this equation to the one given by equation (29).

4.3. INVERSE SOLUTION TO THE CHARACTERISTICS EQUATIONS

As discussed earlier, elastic BCs are introduced in order to better represent the beam dynamics, including the imperfection of clamping at the end points. On the other hand, finding the translational and torsional equivalent spring constants (β_1, β_2, β_3 and β_4) at the end points is a cumbersome practical procedure and sometimes impossible. However, by imposing the experimentally measured natural frequencies of the beam into the characteristic equation (35), one can obtain the parameters β_i. This inverse analysis, which uses the measured frequencies to determine the BCs instead of the other way around, is a realistic way of arriving at beam eigenfunctions for the non-ideal clamped–clamped ends. This

combination of experimental results and theoretical findings is described next and implemented in section 6.

Imposing the first four natural frequencies, the characteristic equation (35) yields a set of simultaneous non-linear algebraic equations in terms of unknowns β_i. For instance, taking into account four modes (four natural frequencies) of the beam, will result in a system of four simultaneous non-linear equations for β_i. Mathematically, the problem can be stated as

$$f_i(\beta_1, \beta_2, \beta_3, \beta_4) = 0, \qquad i = 1, \ldots, 4. \tag{40}$$

The existence and uniqueness of the positive solutions for such a set of non-linear simultaneous equations is almost impossible to prove. Available commercial software, however, can be utilized for a local or global search.

5. EXPERIMENTAL SETTING AND RESULTS

The experimental set-up used to verify the findings is shown in Figure 6. It is the same as that of reference [5]. A brief description is given here for convenience to the reader. The primary structure is a $3/8'' \times 1'' \times 12''$ steel beam (2) clamped at both ends to a granite bed (1). A piezoelectric actuator with a reaction mass (3 and 4) is used to generate the periodic disturbance on the beam. A similar actuator–mass set-up constitutes the DR absorber (5 and 6). They are located symmetrically at one quarter of the length along the beam from the center. The feedback signal used to implement the DR is obtained from the accelerometer (7) mounted on the reaction mass of the absorber structure. The other accelerometer (8) attached to the beam is only to monitor the vibrations of the beam and to evaluate the performance of the DR absorber in suppressing them. The details of this description is left to the article referenced above. The numerical values for this beam–absorber–exciter set-up are given in Appendix B.

The control is applied via a DSP using a sampling rate of 50 kHz in all the experiments presented. The DSP runs the DR routine in a single input–single output mode as a free standing CPU as long as $g(\omega)$ and $\tau(\omega)$ values are unchanged, i.e., ω is fixed. When changed, the variation of ω is measured via the DR acceleration feedback signal. This frequency is utilized to find the gain and delay using equations (4) and (5). It is important to note again that the control loop is closed within the DR structure itself, without external information from the primary. That is, the DR absorber can operate as a *free standing* element to be attached at a point where the vibration needs to be suppressed.

6. DYNAMIC SIMULATION AND COMPARISON WITH EXPERIMENTS

As indicated earlier, the research group of the authors has studied the beam dynamics using the finite difference method (FDM) [5]. This model produced a system stability picture which is not in full concurrence with the experimental counterparts. One particular point of interest appeared when the DR is operating in a dual frequency mode (i.e., the Dual Frequency Fixed Delayed Resonator,

DFFDR). In this mode the DR is tuned to resonate not only at one frequency but two, concurrently. Consequently, the controlled structure, DFFDR, would become an ideal vibration absorber at these two frequencies. The experiments showed a stable combined system and led to expected vibration absorption at both frequencies, while the FDM of the dynamics indicated an unstable operation.

Another difficulty in the earlier FDM study was associated with the determination of the modulus of elasticity, E. These models used ideal clamped–clamped BCs. Consequently a very low E constant was calculated using the first natural mode of the beam and its frequency. Because the clamped–clamped boundary conditions are stiffer than designed, the first natural frequency obtained from experiments were matched only by weakening the beam itself, i.e., lowering E.

In this study the beam dynamics is modelled using the modal analysis technique and the catalogue value of E. The beam is considered to have compliant supports, which exhibit both transverse and bending stiffnesses. The unknown stiffnesses are evaluated using the experimentally determined natural frequencies, as explained above, and the eigenfunctions are found using equation (38).

Without loss of generality, we consider the symmetric boundary conditions here for simplicity. That is,

$$k_{\theta L} = k_{\theta R} \Rightarrow \beta_1 = \beta_3, \qquad k_{TL} = k_{TR} \Rightarrow \beta_2 = \beta_4. \tag{41}$$

Equation (35) should support the experimentally found natural frequencies (i.e., the eigenvalues). Inserting this condition one obtains

$$f_1(\beta_1, \beta_2, \omega_1) = 0, \qquad f_2(\beta_1, \beta_2, \omega_2) = 0, \tag{42}$$

which are two simultaneous non-linear equations for the unknowns β_1 and β_2. There may be many solutions for $\{\beta_1, \beta_2\}$. Those which yield $\beta_1 > 0$, $\beta_2 > 0$ are the acceptable solutions. For the experimental set-up at hand, the natural frequencies are measured for the first two natural modes, ω_1 and ω_2. These frequencies are obtained much more precisely than those of higher order natural modes. Table 1 offers a comparison between the experimental (*real*) and analytical (*ideal*) clamped–clamped beam natural frequencies. The discrepancies arrive from two sources: the experimental frequencies are structurally damped natural frequencies and they reflect the effect of partially clamped BCs. The theoretical frequencies, on the other hand, are evaluated for an undamped clamped–clamped beam, i.e., $\delta = 0$ and $c = 0$ of equation (20).

TABLE 1

Comparison between experimental and theoretical beam natural frequencies (Hz)

Natural modes	Peak frequencies (experimental)	Natural frequencies (clamped–clamped)
First mode	466·4	545·5
Second mode	1269·2	1506·3

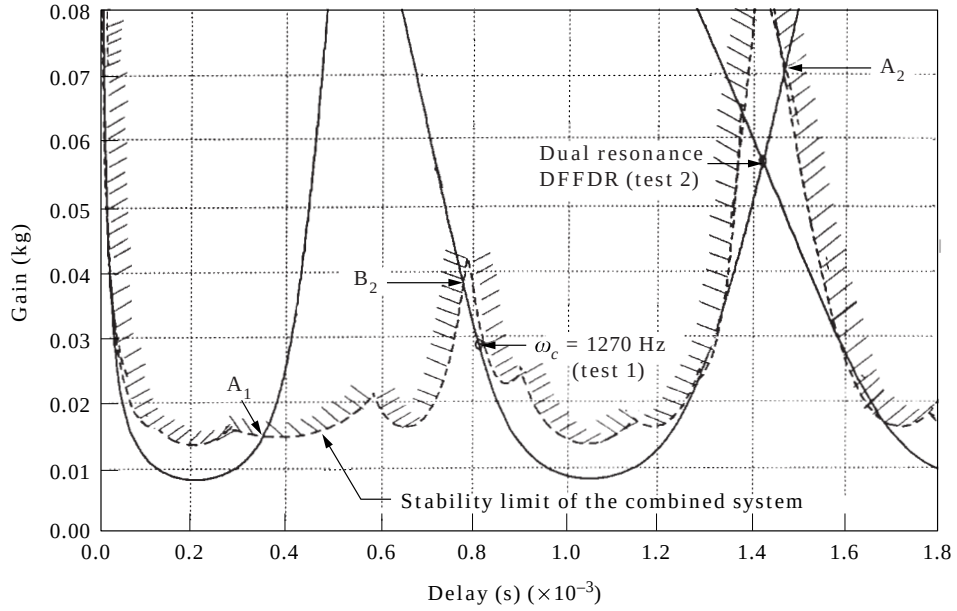

Figure 7. Analytically obtained stability chart: ——, Delayed Resonator; – – –, combined system.

Using the experimental data, and utilizing the Maple symbolic manipulation package for equation (42),

$$\beta_1 = \beta_3 = 22{\cdot}3565, \qquad \beta_2 = \beta_4 = 4530{\cdot}1978 \tag{43}$$

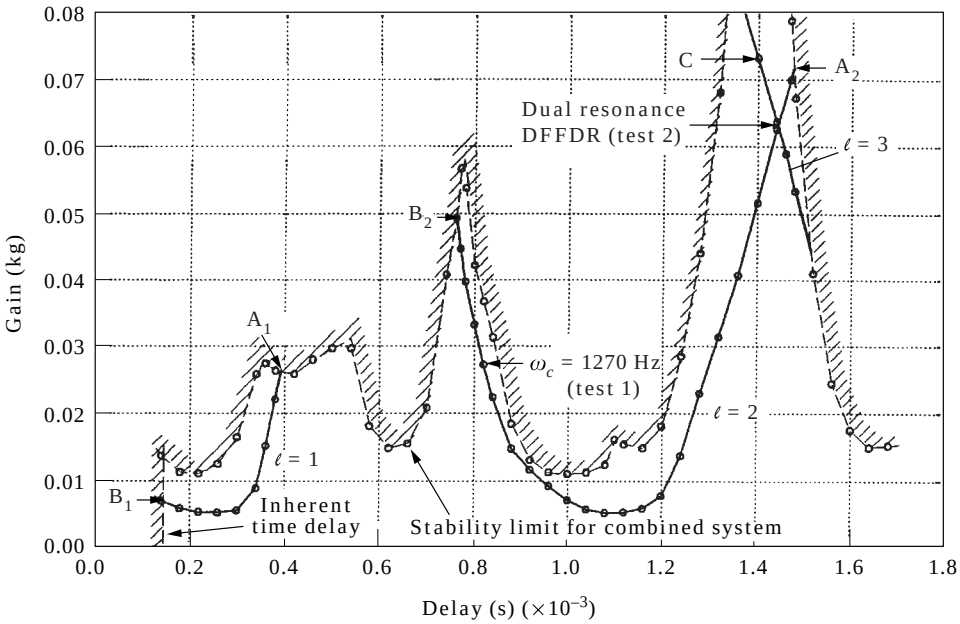

Figure 8. Experimentally obtained stability chart: ——, Delayed Resonator; – – –, combined system.

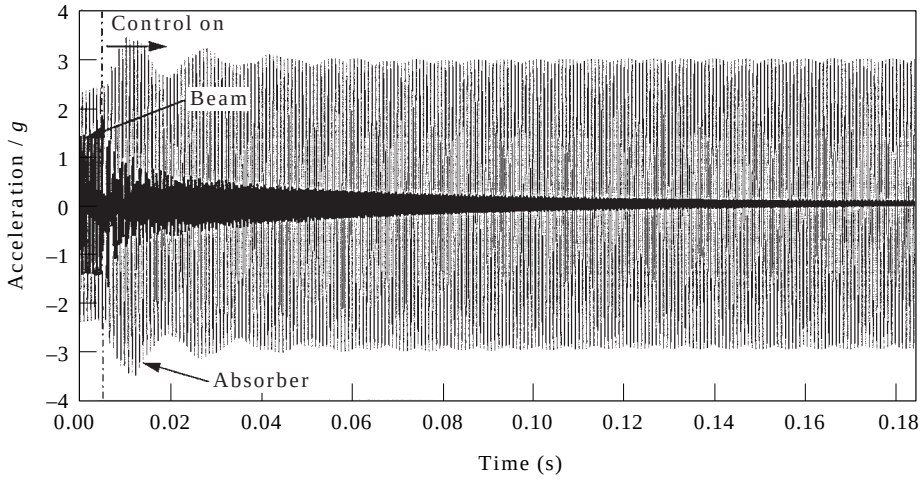

Figure 9. Beam and absorber response to 1270 Hz disturbance, analytical.

are obtained as the realistic stiffnesses. With these values all the modal shapes (i.e., the eigenfunctions), given by equation (42), can be formed. A number of demonstrative exercises arise from this point.

After observing the effect of the number of modes used on the beam deformation, a minimum of three natural modes are taken into account. The first two modes alone do not reveal sufficient detail of the beam deformation for our purposes. This critical selection is made considering the stability of the system. The evolution of the stability curves for the combined system is studied as the number of modes taken in the model increases starting from 3. Figure 7 shows the stability curve resulting from a 3-mode representation. The DR operating points are also shown on this figure with thin lines. Notice that the DFFDR operation remains in the stable side of the curve for the combined system. When the same analysis is performed utilizing the 4-mode representation of the system with the same boundary conditions, no discernible difference in the stability chart is observed. Therefore, for the rest of the study only a 3-mode representation is used.

Next, the same stability tableau from the experiments is presented, Figure 8. The tests which yield this figure are conducted as follows.

For the DR part: the absorber is installed on a vibration isolation table; a fixed delay, τ, is selected; feedback gain, g, is implemented; a pulse excitation force is applied; the time response is observed; g is increased until the system shows "resonant" behavior, say at g_c; the point (τ, g_c) is marked as a "DR operating point"; τ is increased and the above process repeated to cover the region of interest.

For the combined system: (1) the test set-up, as shown in Figure 6, is on a vibration isolation table; (2) τ is selected and implemented, exciter is uncontrolled (i.e., acting as a passive structure); (3) a small gain, g, is applied in DR feedback; (4) the accelerations $\ddot{q}_a$, $\ddot{q}$ (anywhere on the beam) are monitored; (5) g is increased until the combined structure shows marginal stability (i.e., the whole system becomes resonant), say at g_{cs}; (6) the point (τ, g_{cs}) is marked as the stability limit

for the combined system; (7) τ is increased and the above process repeated (from step (1) on) until the entire region of interest ($\tau_{min} < \tau < \tau_{max}$) is covered.

Notice that the point marked as DFFDR is found at the intersection of the first and second branch operations of DR. A very interesting point is that the DR subassembly itself can be unstable (to the left of DFFDR on the third branch such as point C) while the combined system is asymptotically stable.

A good correspondence between Figures 7 and 8 is noticeable. One particular point of interest for us is the fact that the dual frequency fixed delayed resonator (DFFDR) point remains in the stable side (point DFFDR on Figures 7 and 8) of both the analytically and experimentally obtained stability curves. This agreement is one of the critical contributions of this work. It indicates that if the BCs for the primary system were properly selected, the analytical study could reveal the stable operating zones of DR absorption. The method, therefore, constitutes a valuable design tool.

The simulated time response versus the experimental results of vibration suppression are now compared. Figure 9 shows a test with the excitation frequency $\omega_c = 1270$ Hz, which corresponds to point "test 1" in Figure 7. The corresponding theoretical control parameters are: $g_{c\ theory} = 0{\cdot}0252$ kg and $\tau_{c\ theory} = 0{\cdot}8269$ ms. The experimental control parameters for this frequency are found to be $g_{c\ exp.} = 0{\cdot}0273$ kg and $\tau_{c\ exp.} = 0{\cdot}82$ ms (see Figure 8, point "test 1"). The exciter disturbs the beam for 5 ms, then the DR tuning is triggered. The acceleration of the beam at the point of attachment decays exponentially. For all intents and purposes the suppression takes effect in approximately 200 ms. This result matches very closely with the experimental data; Figure 10. The only noticeable difference is in the frequency content of the exponential decay. This property is dictated by the dominant poles of the combined system. It seems that these poles have the same real parts comparing Figures 9 and 10. The imaginary part, however, is smaller in the experimental study. This difference is a small nuance which does not affect the earlier observations.

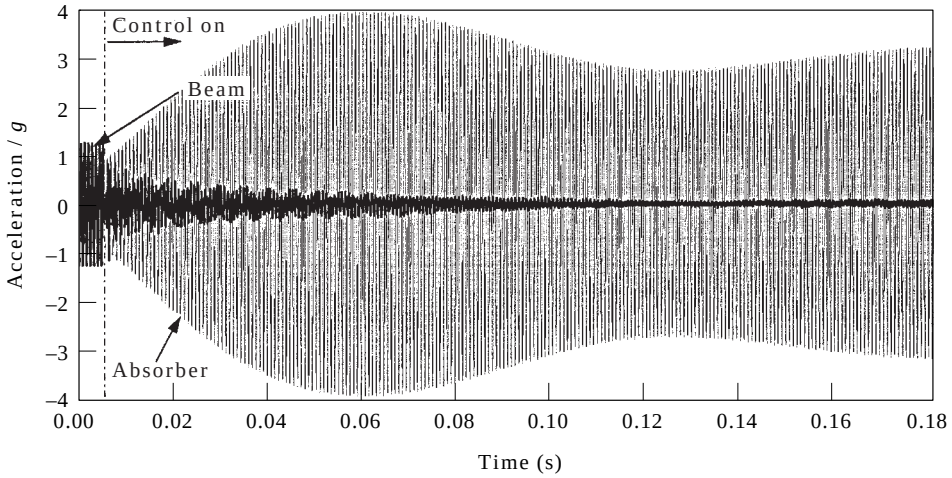

Figure 10. Beam and absorber response to 1270 Hz disturbance, experimental.

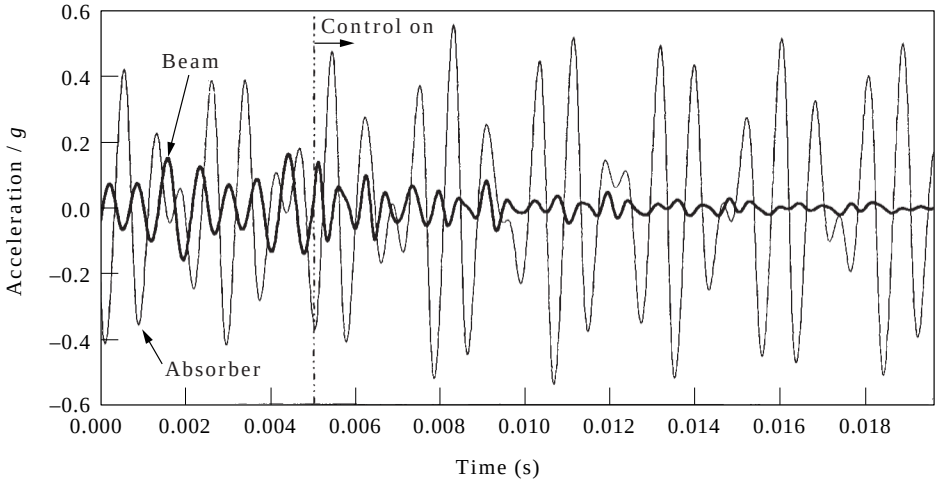

Figure 11. Beam and absorber response to dual frequency disturbance, analytical.

Next, the simulation of DFFDR operation is compared with the experimental results. The operating point is depicted as "test 2" in Figure 7 and the corresponding dual frequency values of the intersection of the second and third Root Locus branches are $\omega_{1theory} = 1037{\cdot}20$ Hz and $\omega_{2theory} = 1422{\cdot}15$ Hz for $g_{c\ theory} = 0{\cdot}0561$ kg and $\tau_{c\ theory} = 1{\cdot}4201$ ms. Corresponding experimental values, respectively, are: $\omega_{1exp.} = 1025$ Hz and $\omega_{2exp.} = 1404$ Hz for $g_{c\ exp.} = 0{\cdot}0623$ kg and $\tau_{c\ exp} = 1{\cdot}424$ ms. The slight difference between the theoretical and experimental values are attributed to the parameter uncertainties and non-linearities of the piezoelectric actuator. Figure 11 shows the beam acceleration at the point of attachment and the DR absorber acceleration, where the exciter is disturbing the beam with a forcing

$$P_1 \sin(\omega_1 t) + P_2 \sin(\omega_2 t). \tag{44}$$

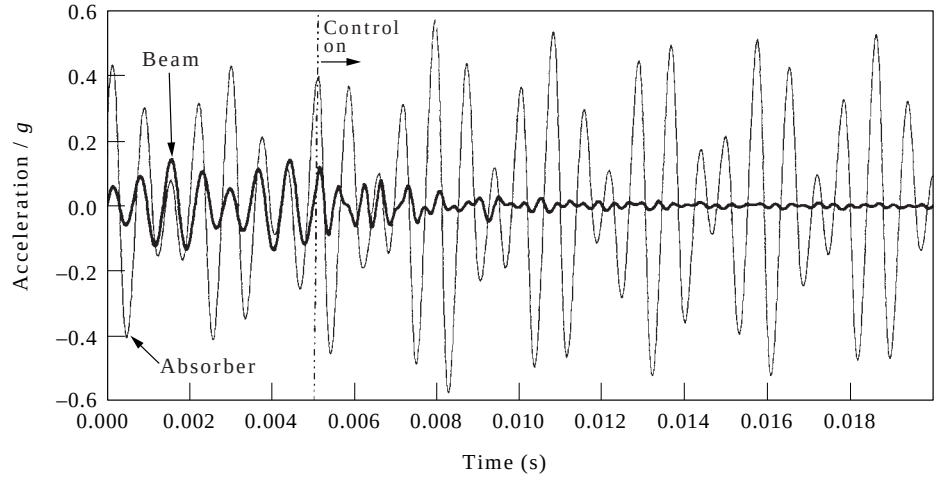

Figure 12. Beam and absorber response to dual frequency disturbance, experimental.

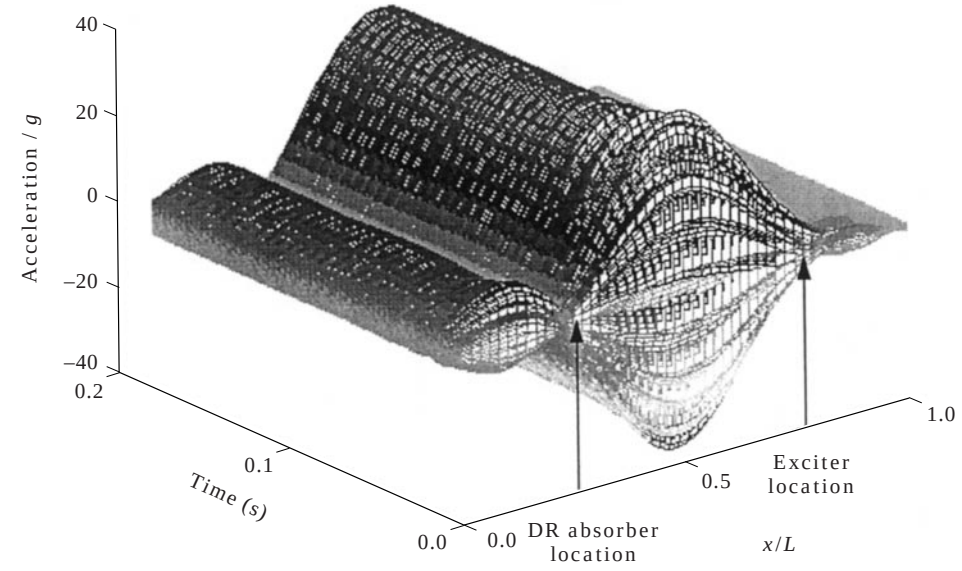

Figure 13. Waterfall depiction of the beam acceleration to 1270 Hz disturbance.

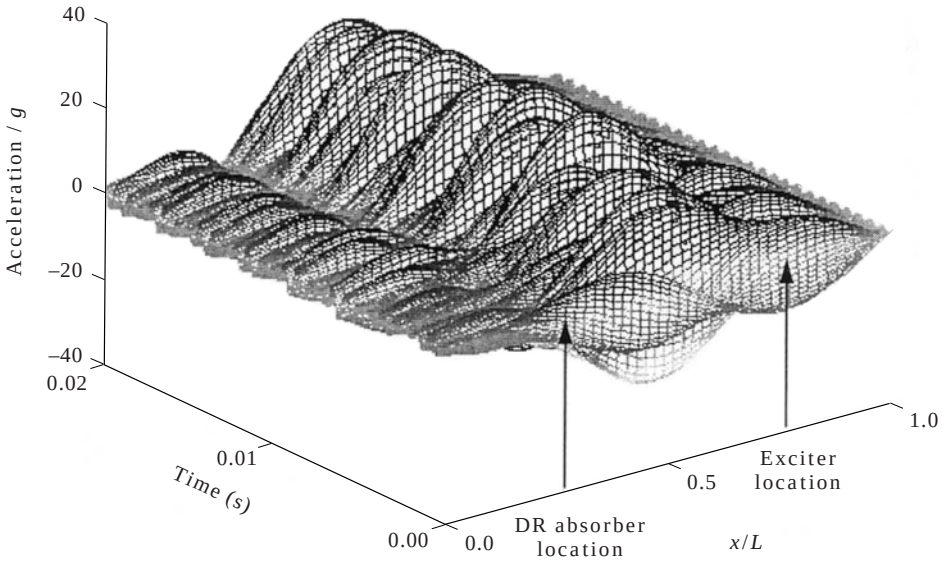

Figure 14. Waterfall depiction of the beam acceleration to dual frequency (1037 and 1422 Hz) disturbance.

Notice the dual frequency trace of the DR once the tuning takes effect at 5 ms, indicating that it is sensitized to resonate at these two frequencies. The suppression appears much faster than it does in Figure 9, because the DFFDR point has a large stability margin (see Figure 7). Figure 12 shows the experimental response of the beam and the absorber to the dual frequency (ω_{1exp} and ω_{2exp}) excitation. The agreement between theoretical and experimental findings is obvious, for this operating condition as well.

Finally, the time trace of each point along the beam is presented using a waterfall depiction; Figure 13 (only beam acceleration is shown). It is clear that the point of attachment gets quieted. Notice that there are some small transverse oscillations and bending slopes at the end points, as expected. A similar picture is presented in Figure 14 for DFFDR operation corresponding to point "test 2" of Figure 7. The bi-tonal signature of the beam acceleration is evident, as well as the fast exponential decay at the point of absorber attachment. Note again that the stability margin is quite high at this point of operation (Figure 7).

7. CONCLUSIONS

A modal analysis representation of a flexible beam is presented. The study is conducted to create an analytical tool for the design of a new tunable vibration absorber, the Delayed Resonator. The details of advantages of the DR absorption method are given in other publications. In this work the correspondence of experimental and analytical findings, especially those which are related to the stability aspects of the combined structure, are treated. An infinite-degree-of-freedom system with a point absorber and a point exciter are taken into account. Both experimental and analytical results are presented. In particular the stable operation of DFFDR (dual frequency) absorption is shown matching the experimental findings. This is a feature which could not be brought to an agreement in the earlier analytical–experimental comparisons. The adoption of the realistic boundary conditions in this study offered a significant improvement as opposed to the ideal clamped–clamped BCs. This approach is, therefore, recommended as a tool for the design of a DR vibration absorber.

ACKNOWLEDGMENT

The authors acknowledge the financial support of NSF under award no. CMS-9415428, and ONR support through Electric Boat. The valuable contributions of Mr Mark Renzulli for the experimental work are much appreciated.

REFERENCES

1. N. Olgac 1995 *U.S. Patent* 5,431,261. Delayed resonators as active dynamic absorbers.
2. N. Olgac and B. Holm-Hansen 1994 *Journal of Sound and Vibration* **176**, 93–104. A novel active vibration absorption technique: delayed resonator.

3. N. Olgac and B. Holm-Hansen 1995 *ASME Journal of Dynamic Systems, Measurement, and Control* **117**, 513–519. Tunable active vibration absorber: the delayed resonator.
4. N. Olgac, H. Elmali and S. Vijayan 1996 *Journal of Sound and Vibration* **189**, 355–367. Introduction to Dual Frequency Fixed Delayed Resonator (DFFDR).
5. N. Olgac, H. Elmali, M. Hosek and M. Renzulli 1997 *ASME Journal of Dynamic Systems, Measurement, and Control* **119**, 380–389. Active vibration control of distributed systems using delayed resonator with acceleration feedback.
6. N. Olgac 1996 *U.S. Patent* 5,502,282. Single mass dual frequency fixed delayed resonator.
7. D. J. Inman 1989 *Vibration: With Control, Measurement and Stability*. Englewood Cliffs, NJ: Prentice-Hall.
8. D. J. Inman 1994 *Engineering Vibration*. Englewood Cliffs, NJ: Prentice-Hall.
9. L. Meirovitch 1986 *Elements of Vibration Analysis*. New York, NY: McGraw-Hill.
10. W. T. Thomson 1981 *Theory of Vibration with Applications*. Englewood Cliffs, NJ: Prentice-Hall.
11. N. Olgac and M. Hosek 1996 *ASME Journal of Vibration and Acoustics* **119**, 131–136. Active vibration absorption using delayed resonator with relative position measurement.
12. S. S. Rao 1995 *Mechanical Vibration*. Reading, MA: Addison-Wesley; 3rd edition.
13. C. M. Harris 1996 *Shock and Vibration Handbook*. New York, NY: McGraw-Hill; 4th edition.
14. S. Y. Lee and S. M. Lin 1996 *ASME Journal of Applied Mechanics* **63**, 474–478. Dynamic analysis of nonuniform beams with time-dependent elastic boundary conditions.

APPENDIX A: COEFFICIENTS OF THE COMBINED SYSTEM CHARACTERISTIC EQUATION

The coefficients of the characteristic equation (35) are all functions of non-dimensional natural frequency $\kappa_i L$, which are defined below.

$$\tilde{a} = 1 - CCh, \qquad \tilde{b} = (\kappa L)^3(SCh + CSh),$$

$$\tilde{c} = \kappa L(SCh - CSh), \qquad \tilde{d} = (\kappa L)^4(1 + CCh),$$

$$\tilde{e} = 2(\kappa L)^4 CCh, \qquad \tilde{f} = -2(\kappa L)^6 SSh,$$

$$\tilde{g} = 2(\kappa L)^2 SSh, \qquad \tilde{h} = -(\kappa L)^7(SCh + CSh),$$

$$\tilde{k} = (\kappa L)^5(CSh - SCh), \qquad \tilde{l} = (\kappa L)^8(1 - CCh).$$

APPENDIX B: THE NUMERICAL VALUES FOR THE BEAM–ABSORBER–EXCITER SET-UP

Beam: $E = 210$ Gpa, $\rho = 1{\cdot}8895$ kg/m.
Absorber: $m_a = 0{\cdot}183$ kg, $k_a = 10130$ kN/m, $c_a = 62{\cdot}25$ N s/m, $a = L/4$.
Exciter: $m_e = 0{\cdot}173$ kg, $k_e = 6426$ kN/m, $c_e = 3{\cdot}2$ N s/m, $b = 3L/4$.

APPENDIX C: NOMENCLATURE

A cross-sectional area of the beam (m^2)
a location of the DR (m)

b	location of the exciter (m)
c	beam damping coefficient (N s/m)
c_a	absorber damping coefficient (N s/m)
c_e	exciter damping coefficient (N s/m)
E	beam modulus of elasticity (Pa)
$\mathbf{F}$	force vector $\{N\}$
g	feedback gain (kg)
g_c	crossing gain for DR (kg)
g_{cs}	crossing gain for combined system (kg)
I	beam cross-sectional of moment of inertia (kg m^2)
k_a	absorber spring stiffness (N/m)
k_e	exciter spring stiffness (N/m)
L	beam length (m)
m	beam mass (kg)
m_a	absorber mass (kg)
m_e	exciter mass (kg)
N_i	generalized beam mass for ith mode (kg)
P	amplitude of constant harmonic force excitation (N)
q_a	absorber displacement (m)
q_e	exciter displacement (m)
q_{bi}	time dependent generalized co-ordinate for the ith mode of beam (m)
S_i	generalized stiffness of the beam (N/m)
t	time (s)
T	total kinetic energy (N m)
U	total potential energy (N m)
x	distance of the beam element from the support (m)
$y(x, t)$	transverse deflection of the beam (m)
$\Phi_i(x)$	mode shape for the ith mode of vibration (-)
ω_{cs}	combined system crossing frequency (Hz)
ω_c	DR crossing frequency (Hz)
ω_{na}	absorber natural frequency (Hz)
ω_i	ith natural frequency of the beam (Hz)
ρ	beam linear mass density (kg/m)
τ	feedback delay (s)
τ_c	crossing delay for DR (s)
τ_{cs}	crossing delay for combined system (s)